Aerodynamic Assessment of a Propeller-Driven, Battery-Electric Large Transport Aircraft with Distributed Propulsion

Dennis Keller,[‡⋆] *Niko Bier,*[‡] *Reynard de Vries,*[†] *and Rob E. Wolleswinkel*[†]
[‡]*Institute of Aerodynamics and Flow Technology, German Aerospace Center (DLR),*
Lilienthalplatz 7, 38108 Braunschweig, Germany
[†]*Elysian Aircraft,*
Hoeksteen 40, 2132MS Hoofddorp, The Netherlands
dennis.keller@dlr.de · niko.bier@dlr.de·
reynard@elysianaircraft.com · rob@elysianaircraft.com
[⋆]Corresponding author

Abstract

With the E9X, Elysian Aircraft aims to develop a battery-electric aircraft for 90 passengers and a useful range of 800 km, equivalent to 430 NM. Comparing these values to the estimations from recently published conceptual aircraft design studies [1], this goal appears challenging. Elysian Aircraft's conviction that it can nevertheless achieve these targets is based on the view that four misconceptions lead to the rather cautious prevailing assessments to date. One of those relates to the aerodynamic performance in particular during cruise flight. In contrast to assumptions of achievable lift-to-drag ratios for this type of aircraft lying between 14 to 18, Elysian Aircraft aims to achieve a comparably high lift-to-drag ratio of around 23 at mid cruise conditions [1]. While this target seems ambitious in itself, there is the additional challenge of enabling sufficient high-lift performance of $C_{L,max} \approx 2.5$ in order to achieve the desired approach category C. The present paper gives an overview on the work that has been performed in order to support Elysian Aircraft's initial assumption that a lift-to-drag ratio of 23 can indeed be achieved by such a configuration. Starting from a conceptual design, a preliminary aerodynamic design of the wing and the propellers was carried out. RANS simulations have then been performed to evaluate the aerodynamic performance of the configuration, also considering the propeller-wing interaction. Further RANS-based design studies allowed the introduction of local wing shape modifications and an improved aerodynamic nacelle design, eventually showing the potential to indeed achieve the targeted lift-to-drag ratio. The aerodynamic potential of high-lift systems with varying complexity ranging from plain flaps to double-slotted fixed-vane flaps has been investigated in order to meet this requirement. The paper gives insight into the high-lift design approach based on sectional and lifting line optimizations followed by an aerodynamic analysis utilizing RANS simulations. The limitations of plain flaps and the potential of slotted flaps to meet Elysian Aircraft's aerodynamic requirements are illustrated for the present aircraft design. In summary, the studies show that Elysian Aircraft's aerodynamic assumptions appear to be reasonable and that there is the potential to actually achieve the required aerodynamic objectives. The integration of the nacelles thereby plays a central role in achieving a suitable compromise between cruise and high-lift.

Nomenclature

Roman Symbols

$\dot{m}$	mass flow rate	kg/s
b	wing span	m
C_p	pressure coefficient, $\frac{p-p_\infty}{q_\infty}$	
C_D	drag coefficient, $\frac{D}{q_\infty S_{\text{ref}}}$	
C_L	lift coefficient, $\frac{L}{q_\infty S_{\text{ref}}}$	
C_T	thrust coefficient, $\frac{T}{\rho_\infty n^2 D^4}$	
D	drag force	N
i_p	propeller incidence angle	deg
L	lift force	N
p	pressure	Pa
q	dynamic pressure, $\frac{\rho V^2}{2}$	Pa
S	surface area	m^2
T	thrust	N
T_t	total temperature	K
V	velocity	m/s

X	roll axis	m
Y	pitch axis	m
Z	yaw axis	m

Greek Symbols

α	angle of attack	deg
δ_{A}	aileron deflection	deg
δ_{F}	flap deflection	deg
η	dimensionless spanwise coordinate, $\frac{2Y}{b}$	
γ	descent angle	deg
ρ	density	kg/m^3

Acronyms

∞	free stream
eff	effective force coefficients that include the propeller blade forces
HEX	heat exchanger
i	individual
loc	local
prop	propeller
ref	reference
xa	roll axis in aerodynamic coordinate system
za	yaw axis in aerodynamic coordinate system
MLG-F	main landing gear fairing

1. Introduction

In order to meet the objective of a more sustainable aviation many approaches such as sustainable aviation fuels, hydrogen propulsion, and battery-electric propulsion are followed. Due to the comparably low energy density of batteries, the latter is usually only considered for the replacement of conventional regional aircraft flying short ranges with passenger numbers of up to 50, at most. This perspective however is challenged by Elysian Aircraft. Its aim is to design an aircraft with a payload of 90 pax and a useful range of 800 km and thus significantly expanding the usually assumed payload-range limitations. With the gravimetric energy density of batteries certainly remaining low for the foreseeable future, energy efficiency becomes a key pillar to achieve this objective. The aerodynamic performance thereby is one fundamental part in the process of converting electric energy into transport work. Elysian Aircraft is building on achieving a lift-to-drag ratio of 23 in cruise flight for its E9X aircraft concept, which is substantially higher than typical values seen for propeller driven tube-and-wing configurations [1]. Additionally, the company anticipates a maximum lift coefficient of 2.5 in approach/landing. While this may not sound overly high, the peculiarities in conjunction with the underlying conditions of the design still make it challenging. The present paper describes the work carried out in order to assess Elysian Aircraft's assumptions regarding the E9X's aerodynamic performance. Starting from a conceptual design, a preliminary aerodynamic design of the wing and the propellers was carried out. RANS simulations have then been performed to evaluate the aerodynamic performance of the configuration, also considering the propeller-wing interaction. Several substudies addressed the design and integration of the main landing gear fairing and the nacelles. Additionally, high-lift systems with varying complexity ranging from plain flaps to double-slotted fixed-vane flaps have been investigated for their potential to meet the initial assumptions regarding low speed performance. The paper gives insight into the high-lift design approach based on sectional and lifting line optimizations followed by an aerodynamic analysis utilizing RANS simulations.

2. Numerical Methods

2.1 Reynolds-averaged Navier-Stokes (RANS)

The numerical simulations based on the Reynolds-averaged Navier-Stokes (RANS) equations have been carried out with the *DLR TAU* code [2]. The code relies on an unstructured finite volume approach for solving the RANS equations. For the present investigation, the implicit LU-SGS scheme was used for time stepping and a central scheme and second order Roe upwind scheme for the spatial discretization of the inviscid mean flow fluxes and the turbulent convective fluxes, respectively. The turbulence effects were modeled with the Spalart-Allmaras formulation (SA) [3] with vortical and rotational flow correction based on the Spalart-Shur correction [4] as well as QCR extension [5]. In order to model the propeller effects, an actuator disk approach based on 2D blade element momentum theory is implemented in *TAU*. In this way, the local forces of the propeller are calculated based on the blade properties and the local flow conditions. Detailed information on the actuator disk implementation can be found in [6]. The actuator disk model has shown robust behavior and good results in terms of performance parameters as well as slipstream velocity distributions for various applications such as the simulations of conventional propellers [7, 8] and contra-rotating open rotors [9].

2.1.1 Meshing

The meshes for the 3D RANS computations were created with a semi-automated hybrid meshing approach using ANSA [10]. ANSA first creates a quad-dominated surface mesh. From the surface grid, a near-field volume mesh is generated with an advancing-layer algorithm to resolve the boundary layers. Due to the characteristics of the surface mesh, the near-field mesh mainly consists of hexahedra stacks with additional stacks of prisms. The outer part of the computational domain is filled with hexahedra, which are growing in size towards the outer domain boundaries. To allow for the growth without hanging nodes, so-called buffer zones, consisting of tetrahedra, are introduced between the hexahedra of different size. The cell sizes of the surface mesh are controlled by geometric features. Moreover, the discretization of the surface mesh as well as the volume mesh can be adjusted via size-fields. The meshes were created based on in-house best practice rules resulting in mesh sizes of approximately 70 million nodes for the cruise configuration and up to 120 million nodes for the configurations with single slotted flaps.

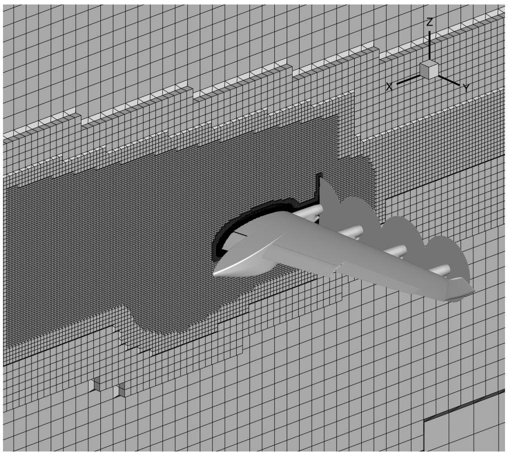

Figure 1: Geometry of landing configuration with volume mesh visualization in z = const cutting plane

2.1.2 Boundary Conditions / Performance Assessment

The following section describes the conditions that were directly - or indirectly via iterative procedures - applied to the computational boundaries other than viscous walls and the symmetry plane.

Actuator Disk The aerodynamic performance of the cruise flight as well as the high-lift configurations was assessed both with and without propeller effects. With propeller effects the thrust was set depending on the configuration:

- **Cruise configuration:** The propeller thrust is set to balance out the drag in horizontal flight. The required thrust was thereby estimated at the design mid cruise lift coefficient. Lift and total propeller thrust were adjusted by variation of the angle of attack and the blade pitch angles at constant propeller RPM until the forces in vertical (equation 1) and horizontal (equation 2) direction were balanced. Since only wing-body geometries were simulated with RANS, an additional drag penalty for the tail was added to the total drag that had to be balanced out. The zero lift component of this drag penalty is based on the conceptual aircraft design data. Additionally, a trim drag for the HTP was estimated based on the prior iteration of RANS computations.
- **Take-off configuration:** A target thrust was given by the conceptual design.
- **Landing configuration:** The utilized thrust was estimated at the design approach lift coefficient. Similar to the cruise flight case, lift and total propeller thrust were adjusted by variation of the angle of attack and the blade pitch angles at constant propeller RPM at a descent angle of $\gamma = -3°$. Again, additional drag penalties for the tail and the landing gear were added to the total drag that had to be balanced out.

$$\begin{aligned}
\Sigma F_{za} &= 0 = L + \Sigma T_i sin(\alpha_{Ti}) - W cos(\gamma) && (1)\\
\Sigma F_{xa} &= 0 = D - \Sigma T_i cos(\alpha_{Ti}) + W sin(\gamma) && (2)\\
\alpha_{Ti} &= \alpha + i_{pi} && (3)\\
\Sigma T_i &= T_{req} && (4)
\end{aligned}$$

Heat Exchanger Inlet/Exhaust Planes Parallel to the aerodynamic assessment, an initial design of the heat exchangers was carried out by partners [11]. The HEX design envisages a variable nozzle to adjust the mass flow rate to the varying flight conditions. The HEX inlet is considered to be fixed. The resulting HEX dimensions were incorporated into the airframe shape. Moreover the boundary conditions at the inlet and exhaust interfaces in terms of mass flow rates, and temperatures that were used in the aerodynamic investigation are based on the HEX design. The mass flow rates were set at the corresponding design operating point in take-off and cruise flight. For the α-sweeps the inlet pressure and exhaust total pressure were kept constant leading to a slightly altering mass flow rate with changing angle of attack. These HEX interface conditions were also used to consider the internal drag of the HEX in the aerodynamic performance assessment.

Table 1 summarizes the boundary conditions used in the RANS computations.

Parameter	**Cruise**	**Take-Off**	**Landing**
Farfield	$C_L = 0.53 - C_{T_{za}}$, α-sweep	$C_L = 1.46 - C_{T_{za}}$, α-sweep	$C_{L,\text{eff}} - C_{T_{za}} = 1.48$, α-sweep
Propeller Setting	balanced drag	$T_{prop} = 17.2\,kN$	balanced drag @ $\gamma = -3°$
HEX inlet[1]	$\dot{m}_{HEX} = 0.96\,\text{kg/s}$	$\dot{m}_{HEX} = 1.23\,\text{kg/s}$	flow through
HEX exhaust[1]	$\dot{m}_{HEX} = 0.96\,\text{kg/s}$, $T_t = 278.35\,\text{K}$	$\dot{m}_{HEX} = 1.23\,\text{kg/s}$, $T_t = 344.45\,\text{K}$	flow through

Table 1: Boundary conditions for performance assessment

2.2 Extended Non-Linear Lifting Line (ENLLL)

The extended non-linear lifting line (ENLLL) method used in this study [12] is similar to van Dam's [13] modified Weissinger method that combines Weissinger's extended lifting line method [14] with an iterative procedure to account for non-linear viscous effects. Therefore, this approach uses 2-D sectional data, which can be derived from various sources. In the present study, the sectional data originate from 2-D RANS computations. The capabilities of this approach have also been demonstrated in more detail by Gallay and Laurendeau [15].

3. Conceptual Design

Elysian Aircraft started the E9X project with the aim of designing a cost-effective zero emission aircraft that can be operated from the same airports as narrowbodies [16]. Several considerations finally led to the top level aircraft requirements provided in table 2 and eventually to the conceptual aircraft design shown in Fig. 2. For the aerodynamic assessment, the most relevant parts of the design obviously are the aircraft dimensions and its shape, which are briefly described as follows and summarized in table 3[2]. The concept is generally driven by the idea of minimizing the empty weight fraction of the aircraft resulting in a rather large wing compared to its fuselage. The aircraft thereby shall fit in the category C airport gates limiting the wing span to 36 m. While the utilization of foldable wingtips allows for a wing span of 42 m, it comes at the cost of larger ailerons compared to a fixed span of 42 m and thus less space for high-lift devices. Moreover, the placement of the main landing gear in the inboard region of the main wing further constrains the spanwise dimensions of the trailing edge devices. As a result, only around 44 % of the wing span can be equipped with flaps adversely affecting the potential maximal high-lift performance.

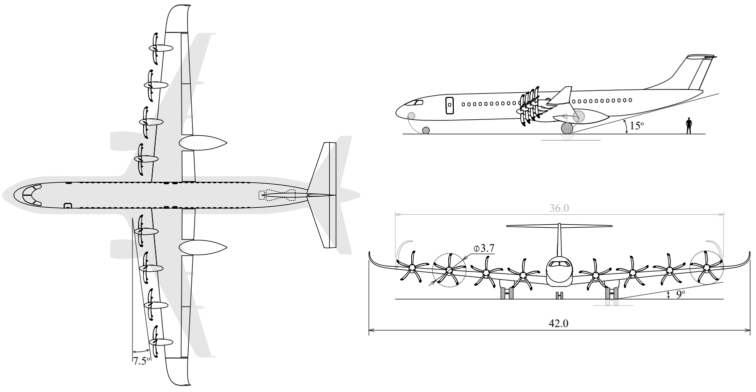

Figure 2: Three-View of E9X

---

[1] The target mass flow rates were only available for the final performance assessment

[2] More information on the conceptual design can be found in [16]

Parameter	Value
Number of passengers [-]	90
Range [km]	800
Take-off field length [m]	2000
Landing distance [m]	2000
Approach speed [m/s]	74.6
Cruise Mach number [-]	0.6
Wing span at gate [m]	< 36

Table 2: Selection of top level aircraft requirements [16]

Parameter	Value
Reference area	148.1 m^2
Span	42 m
Aspect ratio	12.0
Sweep angle (quarter-chord)	2.05°
Mean aerodynamic chord	3.73 m
Propeller diameter	3.7 m

Table 3: Basic geometric properties

4. Results

4.1 Initial Assessment

Subsequent to the preliminary wing and propeller design, an initial assessment of the aerodynamic performance of the cruise configuration as well as the landing configuration was carried out. This design status will be referred to as *baseline*.

4.1.1 Cruise Flight

The initial assessment of the cruise flight configuration was carried out stepwise with consecutively increasing geometric complexity beginning from a wing-body configuration and ending with a wing-body-nacelle geometry including heat exchangers (HEX) and the main landing fairing (MLG-F). The procedure helped to understand the impact of individual components on the total drag as the drag breakdown in Fig. 3 shows for the case at midcruise conditions ($C_L = 0.53$) with propellers off. Accordingly, adding nacelles to the wing-body geometry increases the total drag only by $\Delta C_{D,N} = 0.0006$. However, including the heat exchangers, the contribution increases to a noteworthy $\Delta C_{D,N} = 0.0020$. The MLG-F additionally contributes $\Delta C_{D,M} = 0.0017$ leaving the lift-to-drag ratio of the tail-off baseline configuration excluding internal heat exchanger drag to just above the target with $L/D = 23.1$. With propellers on and thrust trimmed, the lift-to-drag ratio increases to 23.8.

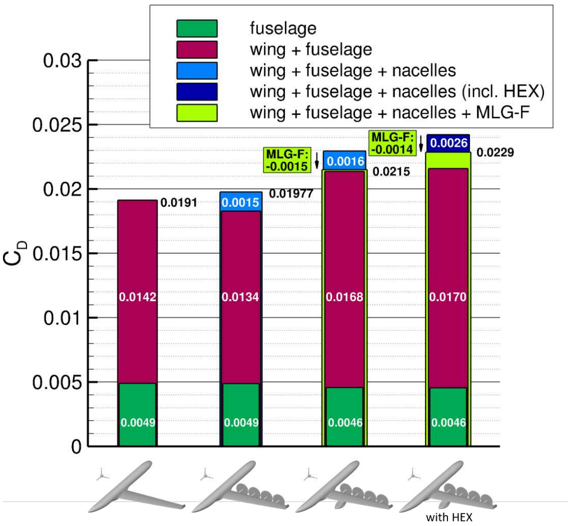

Figure 3: Drag split for initial cruise flight shape with propellers off

4.1.2 High-Lift

A first design of the high-lift system featured plain flaps with a relative chord length of $c_F/c = 0.25$. For the final approach and landing, a flap deflection of $\delta_F = 40°$ was envisaged. The resulting landing configuration however performed rather poor. Figure 4(a) shows the surface pressure (coefficient) distribution and skin friction lines at $\alpha = 9°$ and propellers off. The skin friction lines indicate significant flow diversion on the main wing's upper side downstream of the nacelles. A visualization of the total pressure (Fig. 4(b)) reveals momentum losses linked to vortices caused by the nacelles. Downstream of nacelle 3 and nacelle 4, this effect leads to flow separation. As a result the main wing prematurely stalls leading to a rather poor $C_{L,max}$ of 1.69 for the landing configuration. Moreover, the stall behavior is deemed to be unsatisfactory concerning handling qualities with the flow separation beginning in the outboard region upstream of the ailerons.

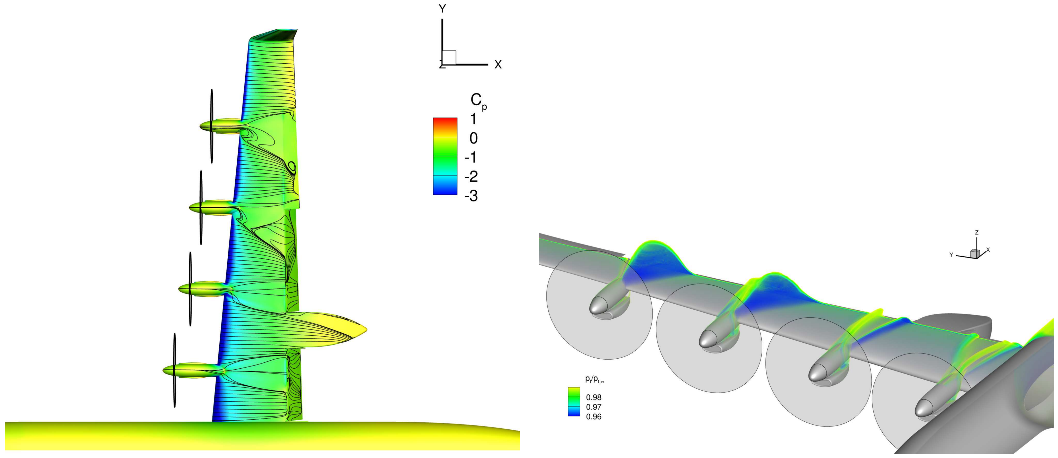

(a) Surface pressure (coefficient) distribution and skin friction lines

(b) Total pressure loss

Figure 4: Stall behavior of initial landing configuration shape with plain flaps at $\alpha = 9°$

4.2 Modifications

4.2.1 Wing Modification

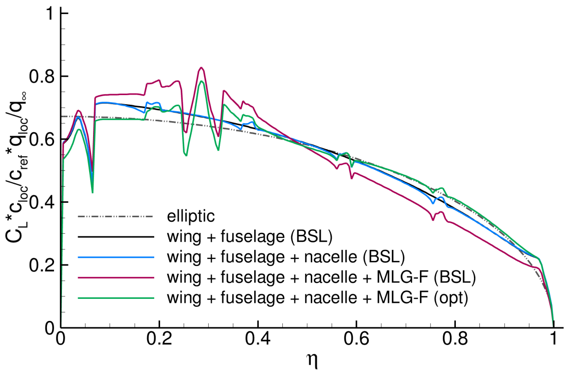

Figure 5: Lift distribution

The analysis of the baseline geometry originating from the preliminary wing design found the main wing's lift distribution slightly diverging from an elliptical one due to a higher load on the inboard wing and consequently a lower load on the outboard wing as shown in Fig. 5 (black line). While considering nacelles (blue line) has little effect on the lift distribution, adding the main landing gear fairing (MLG-F) to the geometry amplifies the lift redistribution towards the inboard region (red line). While the resulting distribution may be favorable in terms of structural design for conventional wings, the impact on structural weight is not yet clear for this concept with the batteries being placed inside the wing. Therefore, it was sought to achieve a more favorable lift distribution with regard to induced drag. For this purpose an optimization of the twist distribution was carried out with the ENLLL method. The important factor here was to take the MLG-F into account during the optimization. The result is represented by the green line that closely matches the elliptic distribution except for the region where the MLG-F is located. The modified twist distributed eventually leads to a drag reduction of $\Delta C_D = -0.0006$.

4.2.2 MLG-Fairing Modification

The shape modification also included a re-design of the main landing gear fairing aiming at the reduction of the zero lift drag on the one hand and a reduction in the overall induced drag on the other hand. For the latter, the cambering of the MLG-F including the local wing section was addressed by modifying the rear droop of the MLG-F. The idea thereby was to affect the local lift in order to flatten out the lift distribution and align it with the elliptical one. Figure 6 illustrates the impact of the camber modification on the MLG-F's surface C_p distribution. From Fig. 6(a) to 6(c) the local cambering is increased. In Fig. 6(b)) lower pressure on the MLG-F's upper surface in proximity to the wing's trailing edge can be observed. In Fig. 6(c) a change in the pressure on the MLG-F's lower surface is more pronounced. Evaluating the lift contribution of the MLG-F component (unclosed surface) to the overall wing at constant airframe C_L indeed indicates an increase in local lift due to the MLG-F as shown in Fig. 7 up to mod. 3. If the cambering is increased beyond the one of mod. 3, the lift contribution slightly decreases. Moreover, the drag coefficient on aircraft level (at constant C_L) increases as well. It has to be noted however that due to time constraints, the study on the MLG-F modification was carried out individually and in parallel to the wing twist optimization. Performing a combined modification/optimization of the wing twist and the MLG-F camber may improve the overall result in terms of C_D. Nevertheless, the basic MLG-F shape modification (mod 1, see Fig. 8) in conjunction with the camber modification yields a drag reduction of $\Delta C_D = -0.0005$.

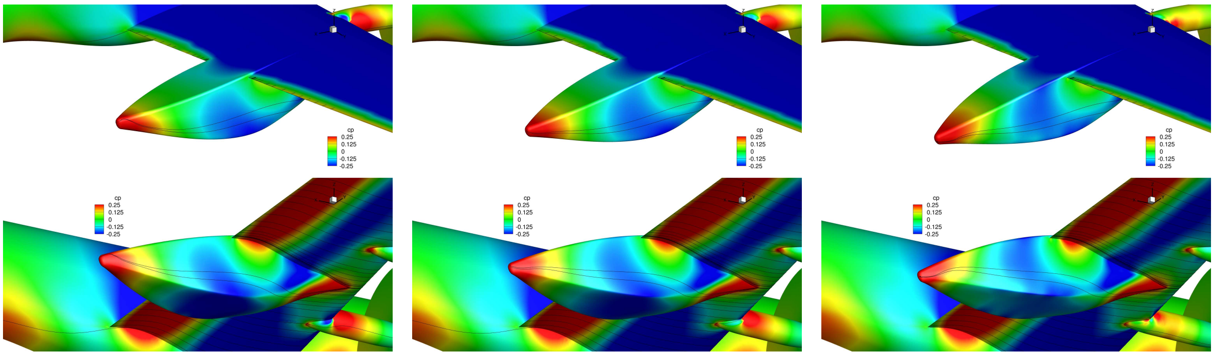

(a) Mod 1 (b) Mod 2 (c) Mod 4

Figure 6: Effect of local cambering via MLG fairing shape by means of surface pressure (coefficient) distribution

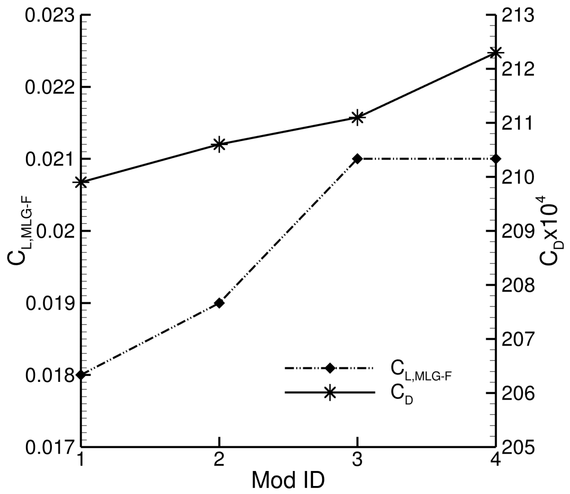

Figure 7: Effect of local cambering via MLG fairing shape on MLG fairing's contribution to C_L and overall C_D

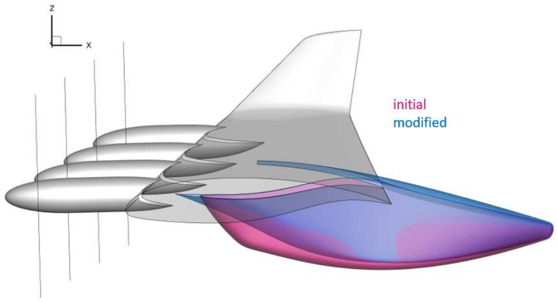

Figure 8: Shape of main landing gear fairing

4.2.3 Nacelle Shape Modification and Nacelle Position

Initially, the nacelles' vertical and streamwise positions were chosen with the aim of minimizing the required propulsive power during cruise flight based on experience from previous design studies. With this objective in mind the selection of the vertical positions are the ones that minimize the cross-sectional area of the wing-nacelles shape. With regard to the streamwise position, the positioning is more complex as several factors counter-act each other. Figure 9 shows the sensitivities of the airframe's lift-to-drag ratio and required propulsive power with regard to the individual streamwise propeller positions neglecting the nacelles. It indicates that the L/D ratio benefits from a slight shift ($-0.25\,m$) of any propeller position in upstream direction. The required power however already decreases for propeller 2. The most beneficial effect can be attributed to the change in position of propeller 1. Increasing the distance to the wing further ($-0.5\,m$) still leads to an increase in L/D in case of propeller 1 and most likely propeller 3. The required power however increases. Considering the adverse affect of increased nacelle drag would further worsen the assessment. Moreover utilizing a propeller staggering philosophy that reduces the impact of any blade-off event prevents moving the outer propeller more upstream than the inner ones. This led to the decision to only move propeller 1 upstream by $-0.25\,m$ yielding a rather small improvement of $\Delta C_D = 0.00005$.

The initial assessment of the high-lift performance indicated premature wing stall due to nacelle induced flow separation. In order to mitigate this phenomenon, a sensitivity study on the vertical propeller/nacelle position and nacelle shape with regard to the maximum angle of attack was performed based on a 3D wing section around propeller 4 with propellers off. The objective thereby was to delay nacelle induced flow separation due to modifications to the shape and position of the nacelle-heat exchanger combination and thus increase both α_{max} and $C_{L,max}$ in low speed. Figure 10 illustrates the effect of basic nacelle shapes on the flow downstream of the nacelle by means of total pressure losses for the baseline vertical position at $\alpha = 8°$. The nacelle without heat exchanger causes significant total pressure losses due to detached flow related to nacelle circulation induced vortices (Fig. 10(a)). Interestingly, adding a podded heat exchanger to the geometry delays the flow separation and thus reduces the total pressure losses at $\alpha = 8°$ (Fig. 10(b)). It appears that the roll up of vorticity of the lifting body namely the nacelle is split into a lower and an upper part with the heat exchanger somewhat shielding the upper part. The effect of the circulation induced vortices of the nacelle can still be observed by means of accumulation of low momentum flow in the wing's upper surface boundary layer downstream of the nacelle. Nevertheless, these losses do not yet lead to flow detachment at this angle of attack. Further integrating the heat exchanger into the nacelle by merging the sidewalls again reduces the maximum angle of attack and leads to flow detachment at $\alpha = 8°$ (Fig. 10(c)). Lastly, modifying the rounded shape of the upper part of the nacelle into a more squared shape as shown in figure 10(d) has the effect of spreading the total pressure losses over a wider spanwise range. While this effect was found to be beneficial under cruise flight conditions it had an adverse effect on the maximum angle of attack in low speed.

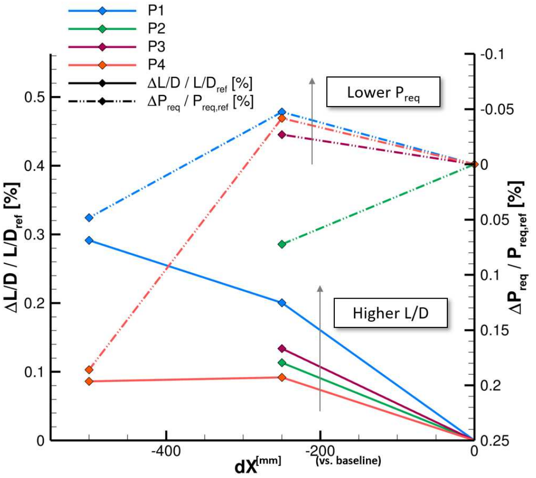

Figure 9: Effect of individual streamwise propeller position on cruise flight performance

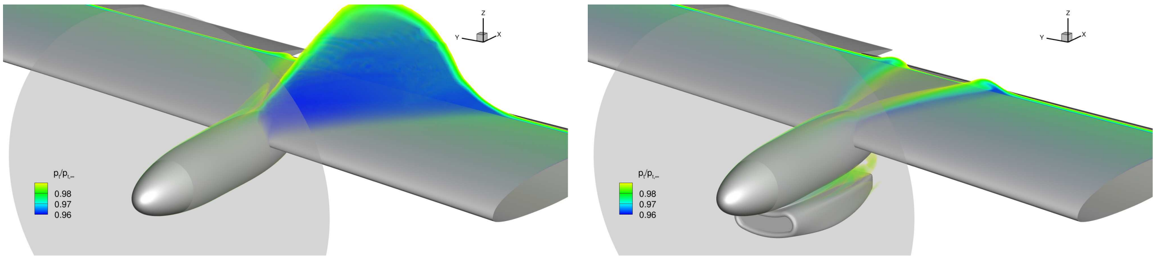

(a) Without heat exchanger

(b) Podded heat exchanger (baseline)

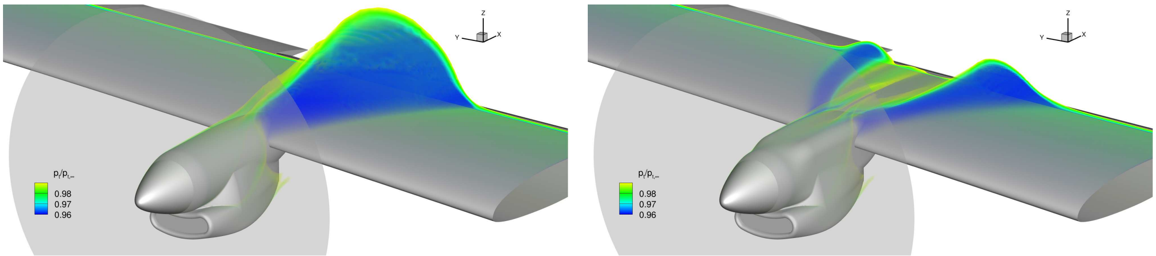

(c) Semi-integrated heat exchanger

(d) Semi-integrated heat exchanger (v2)

Figure 10: Effect of heat exchanger integration on flow downstream of nacelle by means of total pressure loss at $\alpha = 8°$ (based on 3D wing section)

Besides the shape, the nacelle's vertical position has a substantial effect on the flow downstream of the nacelle as demonstrated in Fig. 11 for the baseline nacelle-heat exchanger shape at $\alpha = 10°$. In the baseline case (Fig. 11(a)), the flow is detached downstream of the nacelle indicated by massive total pressure losses. Reducing the vertical position steadily reduces the total pressure losses (Fig. 11(b) and 11(c)). Here, it can be observed that the loss distribution is asymmetrical to the propeller axis and appears to be affected by the wing sweep and the wing-nacelle junction. Moreover, the losses become more distributed along the span with decreasing vertical nacelle position.

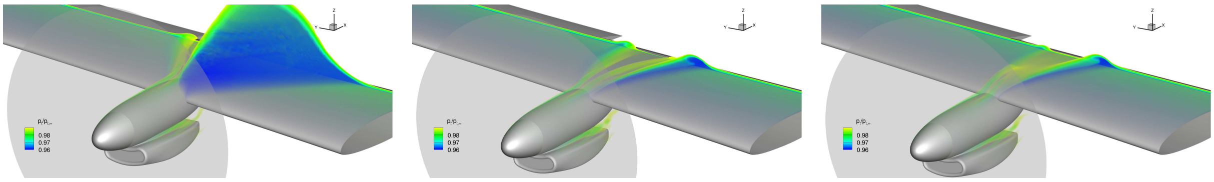

(a) $Z/c = -0.05$ (b) $Z/c = -0.09$ (c) $Z/c = -0.11$

Figure 11: Effect of vertical nacelle position on flow downstream of nacelle by means of total pressure loss at $\alpha = 10°$ (based on 3D wing section)

Figure 12(a) summarizes the effect of the vertical nacelle position on the maximum angle of attack with propellers off based on the 3D wing section. It shows that α_{max} depending on the vertical nacelle position follows a nearly linear trend up to α_{max} of the section without nacelle[3]. It has to be noted however that despite introducing leading edge droop at the outboard symmetry plane to prevent premature stall due to the wall effect in conjunction with the wing sweep initial flow separation occurred in that region in the case without nacelle. Nevertheless, the study demonstrates a significant improvement to α_{max} due to alteration of the vertical nacelle position. This beneficial effect however comes with an adverse effect on the drag in cruise flight as Fig. 12(b) indicates. The drag steadily increases with decreasing nacelle position, whereby the increment decreases with rising angle of attack. For the final design, a trade-off between the low speed benefits and the drawback on cruise flight performance was made for the individual vertical position of each propeller. Despite this trade-off that leads to improved high-lift performance the nacelle/HEX shape and position modification yields a drag reduction in cruise flight of $C_D \approx -0.0015$.

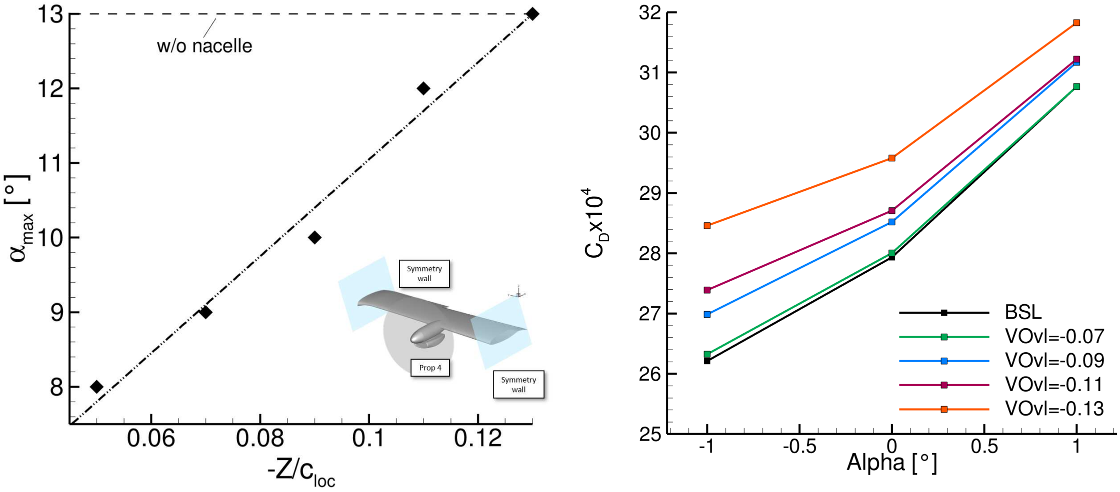

(a) α_{max} in low speed (b) Drag coefficient in cruise flight

Figure 12: Effect of vertical propeller position (based on 3D wing section)

Heat Exchanger Intake In order to assess the heat exchanger intake to be feasible, it has to be ensured that the inlet can provide the required mass flow rate to the radiator over the entire flight trajectory. Moreover, flow separation causing total pressure losses within the inlet or increased drag at design conditions in cruise flight and take-off should be avoided. The cross sectional inlet area is thereby dimensioned by "hot day" conditions during take-off. In this case the required cooling demands, i.e. mass flow rate is high and the onset flow velocities are low [11].

For the mid cruise conditions (Fig. 13(a)) as well as the investigated take-off conditions (Fig. 13(b),13(c), 13(d)), the flow is fully attached to the surface. Even at the maximum angle of attack in take-off (Fig. 13(c)) no flow separation can be observed. At mid cruise, the stagnation line in particular on the lower side is located slightly inside the inlet leading to lower pressure on the lip that reduces the spillage drag. On the upper side, the existence of the nacelle somewhat prevents the stagnation line to move inside the inlet. At the design operating point under take-off conditions, the stagnation line is shifted towards the outboard. As a result, the low pressure zone on the lip is reduced. The inlet has not yet been tested at sideslip angles.

---

[3] The alpha-sweeps were computed with an increment of $\Delta\alpha = 1°$.

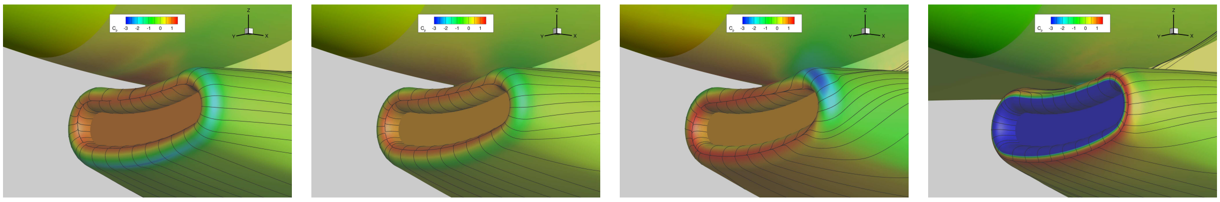

(a) Mid cruise

(b) Take-off at design conditions

(c) Take-off at α_{max}

(d) Take-off with $\dot{m}_{HEX} = 4.94\,kg/s$ ("hot day" conditions) at $M = 0.1$ and $\alpha = 0°$

Figure 13: Surface pressure distribution and skin friction lines at heat exchanger intake of nacelle 1

4.2.4 High-Lift Design: Slotted Flaps

The assessment of the baseline high-lift configuration clearly indicated that the maximum lift coefficient that can be achieved with plain flaps in approach/landing is insufficient. The next step therefore was to moderately increase system complexity by utilizing single-slotted flaps with dropped-hinge kinematics. Several geometric constraints such as minimum vertical hinge-line position, relative flap chord length, and minimum flap thickness were thereby imposed on this type of flap system. Being aware that achieving the targeted $C_{L,max}$ under these constraints will be nonetheless challenging, the high-lift design of the slotted flaps primarily focused on maximizing $C_{L,max}$ in landing configuration and less so on the take-off performance. Initially, the single-slotted flap high-lift system was designed based on numerical optimizations of (2D) wing sections as done before in other projects [17, 18]. Two wing sections representing the regions of the inboard and the midboard flap were therefore individually optimized with the objective of maximizing $C_{L,max}$. To further improve the high-lift performance, optimizations with the ENLLL method in the optimization loop have been performed. With this approach, the shapes of the high-lift system in the two design sections are assessed in parallel within each optimization iteration by means of 2D-RANS computations. The results are then fed into the ENLLL method that computes the high-lift performance on aircraft level. Figure 14 gives an overview on the representation of the E9x maing wing in the ENLLL method. The hatched blue areas thereby indicate the regions, which are fed with the data from the 2D-RANS computations that are performed in every optimization iteration. The remaining regions are fed with either 2D-RANS data that remains identical over the entire optimization or simplified models e.g. for the fuselage and the impact of the main landing gear fairing. Finally, the ENLLL output is evaluated with regard to the optimization's objective function.

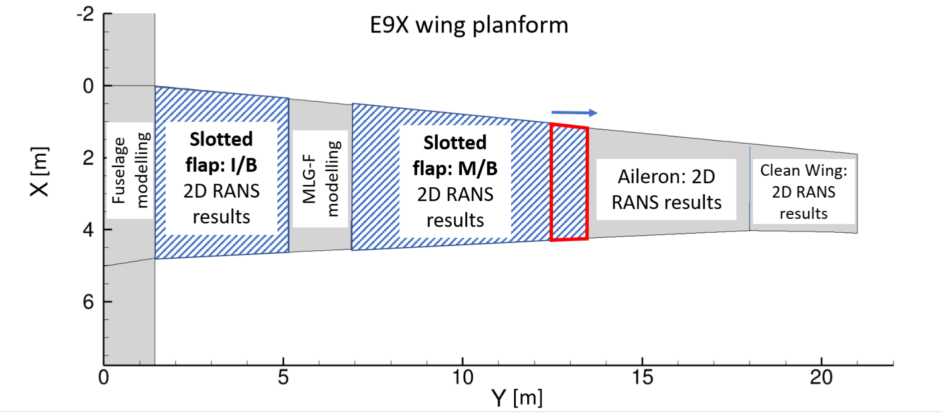

Figure 14: Representation of E9X main wing for high-lift design optimization based on ENLLL

The results of the two optimization approaches regarding $C_{L,max}$ in landing are shown in Fig. 15. The sectional lift curves of the optimized shapes are thereby shown in Fig. 15(a) and 15(b) with the results from the 2D and the ENLLL optimization approaches being represented by red and blue lines, respectively. On aircraft level, the landing configuration of the 3D model resulting from the 2D optimization approach would yield a $C_{L,max}$ of 2.21 based on an ENLLL estimation as shown in Fig. 15(c). This compares to an estimated $C_{L,max}$ of 1.99 for a plain flap design. Comparing the blue lines with the red lines shows that the sectional $C_{L,max}$ values are actually lower for the ENLLL approach. Nevertheless, the $C_{L,max}$ on aircraft level is increased by 7 % to 2.36. The reason for the increased $C_{L,max}$ is that the wing stall is not caused by reaching the maximum angle of attack in any of the high-lift design sections but rather by flow separation on the outboard wing. As a result, the higher $C_{L,max}$ values of the high-lift sections are never reached either. When the wing stalls, the local angle of attack in the design sections is in the linear range, where in fact the values at identical α are higher with the ENLLL approach. Moreover, the ENLLL approach also considers the lift distribution, i.e. the distribution of effective angles of attack along the wing span during the optimization, tendentially relieving the outer wing by reducing the local effective angles of attack as far as possible.

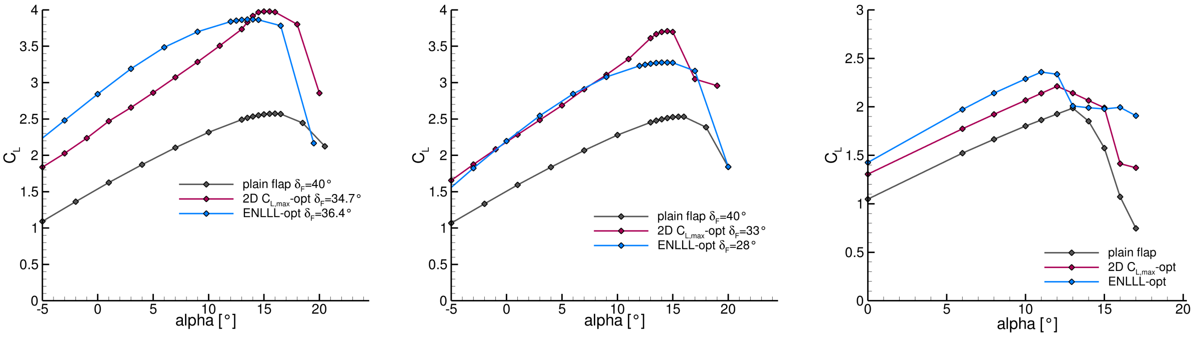

(a) Inboard section (2D) (b) Midboard section (2D) (c) ENLLL estimation

Figure 15: Lift curves of optimized landing configuration depending on optimization approach

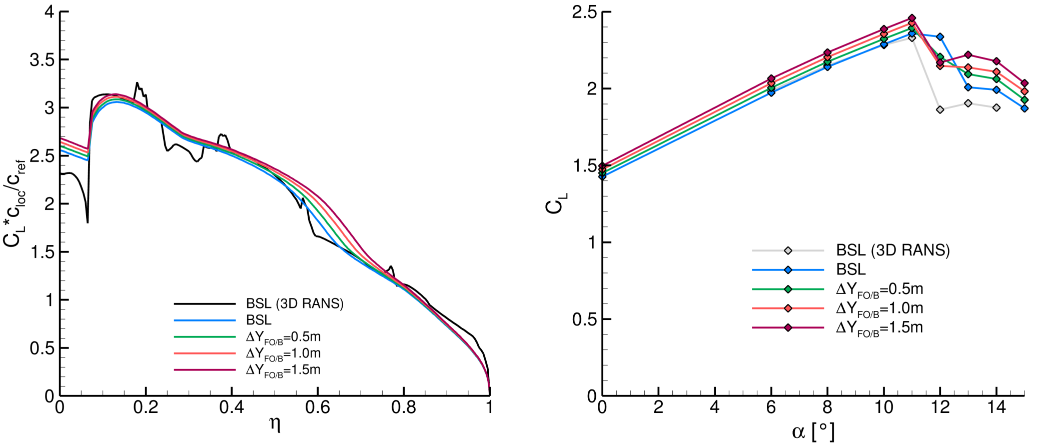

(a) Lift distribution (b) Lift curve

Figure 16: Effect of spanwise flap dimension (based on ENLLL)

As the landing performance was still found to be insufficient, the ENLLL method was used to investigate the potential benefits of an increased spanwise width of the midboard flap as indicated by the red outline in Fig. 14. Figure 16 illustrates the impact of a change in the outer spanwise flap end. As expected, the region with locally increased lift due to the flap system is extended towards the wing tip due to the spanwise flap extension. As a result, the maximum lift coefficient can be increased by $\Delta C_{L,max}/\Delta Y_{F_{O/B}} \approx 0.07\,1/m$.

4.3 Final Assessment

The following section describes the final results of the cruise flight and high-lift configurations subsequent to the modifications.

4.3.1 Cruise Flight

The force balancing at mid cruise conditions resulted in an angle of attack of $\alpha = 0.2°$ and a total thrust (for the half model) of $T_{total} = 16.0\,kN$. Figure 17 depicts the surface pressure (coefficient) distribution and skin friction lines on the upper side of the cruise flight configuration at mid cruise conditions with propellers on. The skin friction lines reveal fully attached flow on the entire main wing, including the MLG-F. Without any additional considerations, the tail-off configuration achieves a lift-to-drag ratio of $L/D = 25.6$ at $C_{L,eff,midCr} = 0.53$ as shown in Fig. 18. Considering the lift and drag penalties related to the tail, the L/D ratio decreases to 23.2. When the internal drag from the heat exchangers is also considered, L/D is further lowered to 22.7, slightly below the target value of 23. The green curve indicates however that the L/D ratio still rises at $C_{L,eff} = 0.53$ with increasing C_L to a maximum of 23.6 in the range between $0.63 \leq C_L \leq 0.75$.

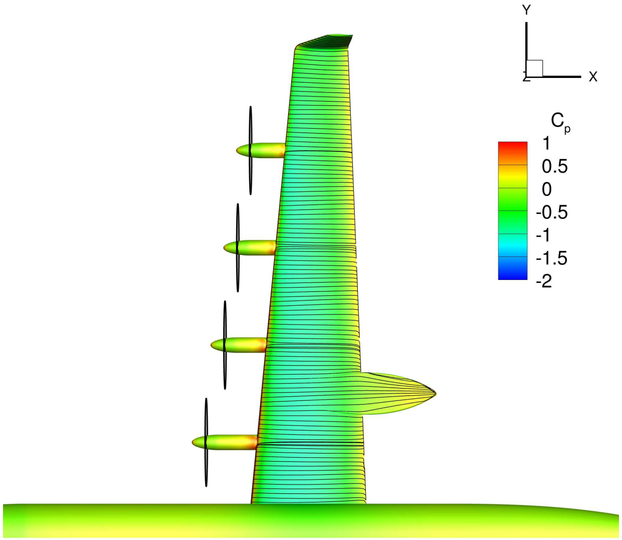

Figure 17: Surface pressure distribution and skin friction lines at mid cruise conditions with propellers on

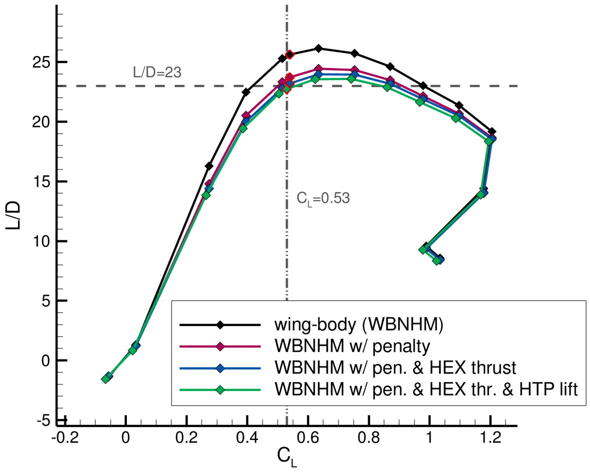

Figure 18: Lift to drag ratio depending on lift coefficient of final cruise flight configuration with propellers on

4.3.2 High-Lift

The final high-lift design results from the approach described in section 4.2.4 and utilizes single-slotted flaps with dropped-hinge kinematics. Moreover, the results from the nacelle design & position studies were used to tailor the stall behavior of the high-lift configurations. For the landing configuration, where only low to moderate thrust levels are expected, the areas of flow separation that trigger the wing stall could successfully be moved towards the inboard wing. In take-off configuration the thrust levels are typically very high and thus affect the stall pattern. Figure 19 visualizes the total pressure deviations compared to the reference total pressure for the take-off configuration at maximum angle of attack. Without propellers the appearance of total pressure losses generally resemble the one seen for the landing configuration as shown for the baseline at post stall in Fig. 4(b) with the highest losses occurring downstream of the nacelles. However, in contrast to the baseline (not shown for α_{max}), the total pressure losses downstream of the inner nacelles 1 and 2 are stronger than the ones downstream of nacelles 3 and 4 due to the modified vertical nacelle positions. With propellers at take-off thrust (Fig. 19(b)) additional regions of increased pressure losses occur between the slipstream regions that are indicated by higher total pressure. Here, the adjacent slipstreams introduce vorticity causing total pressure losses without the beneficial effect of the slipstreams' higher momentum, itself. This happens in a region of high local circulation augmented by the adjacent slipstreams. Lifting line computations support the view that these regions are particularly prone to flow separation even without the additional vorticity introduced by the adjacent slipstreams.

The resulting stall patterns for the high-lift cases are summarized in Fig. 20. The stall patterns for the landing configuration with and without propeller effects as well as for the take-off configuration without propeller effects are very similar and are shown in Fig. 20(a) using the example of the landing configuration without propeller effects. In this case, small areas of trailing edge flow separation exist on the flaps and the aileron at low angles of attack. With rising angle of attack, the flow gradually reattaches to the flaps due to the slat effect of the main wing. At $\alpha = 11°$, larger areas of flow separation occur on the upper side of the aileron that are affected by the wake flow of nacelle 3 and 4. While the flow separation on the aileron will reduce the aileron effectiveness this effect is thought to be manageable. Moreover, the flow detaches from the rear part of the main landing gear fairing. Wing stall is finally triggered by nacelle induced flow separation downstream of nacelle 2 at $\alpha = 13°$.

The take-off configuration with (high) take-off thrust is the only high-lift case deviating from this stall pattern. In this case the additional momentum within the propeller slipstream counter-acts the adverse effect of the nacelle

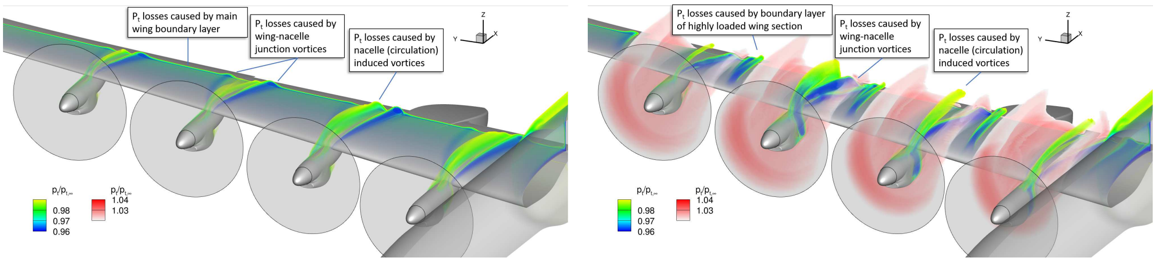

(a) Propellers off

(b) Propellers on

Figure 19: Total pressure losses above main wing in take-off configuration at α_{max}

vortices on the boundary layer momentum distribution. The wing areas outside of the propeller slipstreams are now prone to flow separation as discussed before (Fig. 19(b)). Despite trailing edge flow separation on the flaps at low angles of attack, noteworthy local flow separation begins to emerge at the wing root at moderate angles of attack. Wing stall eventually occurs due to leading edge flow separation between propellers 3 and 4 at $\alpha = 15°$. Obviously, this stall behavior with significant flow separation at the outboard wing, and in particular in the aileron region, is unsatisfying. The outboard flow separation however comes at a relatively high angle of attack and lift coefficient, which are respectively higher than α_{max} and $C_{L,max}$ of the take-off case without propeller effects. As the case without propeller effects (being a conservative representation of engine idle conditions) eventually is the relevant one for certification, the outboard flow separation could be avoided by e.g. utilizing an angle of attack limiter or artificial stall trigger.

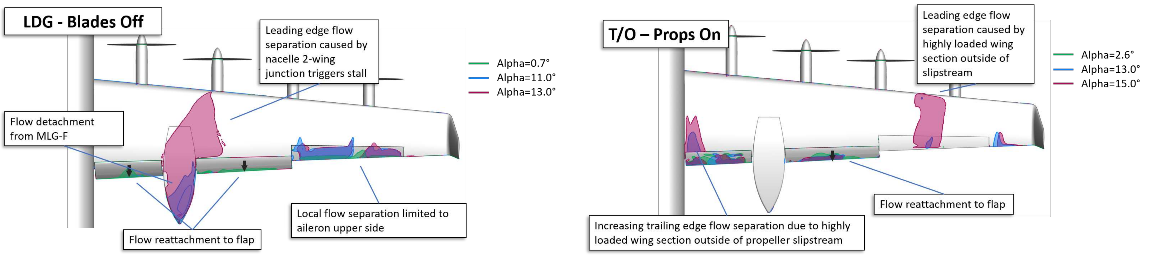

(a) Landing (propellers off propellers on), take-off propellers off

(b) Take-off propellers on

Figure 20: Stall patterns of high lift configurations

Figure 21(a) compares the lift curves of the landing configuration with slotted flaps to the ones with plain flaps obtained from 3D RANS computations. Without propeller effects (solid lines), the slotted flap design yields a maximum lift coefficient of $C_{L,max} = 2.34$, which is an increase by $\Delta C_{L,max} = 0.48$ compared to the plain flap. The figure also demonstrates the effect of the propellers on the lift curve in landing configuration under approach conditions (dash-dotted lines). With plain flaps $C_{L,max}$ and $C_{L,eff,max}$ are increased due to propeller effects by 16 % and 19 %, respectively. With slotted flaps the relative increase is notably smaller with $\Delta C_{L,max}/C_{L,max,POff} = 6\,\%$ ($\Delta C_{L,eff,max}/C_{L,eff,max,POff} = 9\,\%$). The main cause for the smaller increase is related to the varying drag of the two configurations. In the operating point, the drag of the plain flap configuration is substantially higher than the one of the slotted flap. As a result, the required thrust is also higher eventually leading to a stronger lift augmentation.

Further Considerations Figure 21(a) also reveals that the maximum lift coefficient achieved with slotted flaps - when not considering propeller effects - does not fulfill the $C_{L,max}$ target of 2.5. While modifications such as a spanwise flap extension or improved nacelle integration to delay stall may allow to achieve the target with slotted flaps an increase in the high-lift system's complexity was also investigated. The fixed-vane flap is a compromise between the single slotted and double slotted flap as it consists of two flap elements with the smaller one being fixed to the nose of the main flap element. Again the investigated fixed-vane flap was designed as being equipped with dropped hinge kinematics. Figure 21(b) shows the benefits of the fixed-vane flap compared to the slotted flap and plain flap in terms of $C_{L,max}$ in landing configuration without propeller effects. As no final 3D RANS computations were carried out for the fixed-vane design, the lift curve is an estimation based on the ENLLL approach. With the uncertainty around α_{max} prediction with ENLLL, the $C_{L,max}$ is estimated to be between 2.5 and 2.55. Assuming that the estimation is similarly reliable as the ENLLL results for the other high-lift designs, the fixed-vane flap should therefore yield sufficient high-lift performance to deliver on the $C_{L,max}$ target.

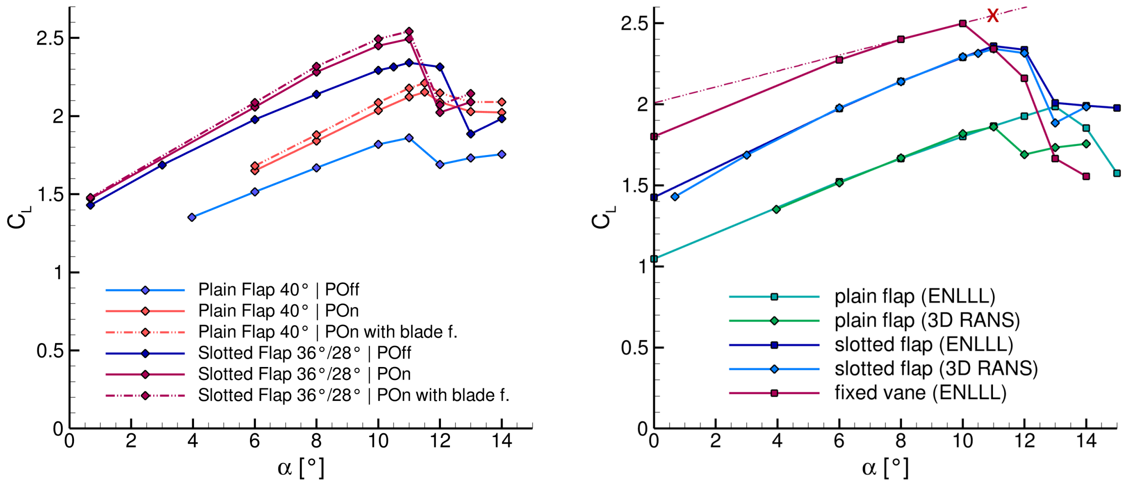

(a) Propeller effect (b) Variation of trailing edge device (propellers off)

Figure 21: Lift curves of landing configuration depending on utilized trailing edge device and propeller effects

5. Conclusion

A comprehensive numerical investigation has been carried out to verify the assumptions from Elysian Aircraft's initial aircraft design with regard to aerodynamic performance of the E9X concept. Therefore, various substudies on aspects such as main landing gear fairing and nacelle shape design and integration, propeller position, high-lift devices were performed utilizing a 3D RANS approach. The final assessment supports the initial assumption that a L/D of 23 is generally feasible in cruise flight with this aircraft concept. However, with only around 44 % of the wing span being utilized by high-lift devices, the initially envisaged high-lift system consisting of plain flaps will not be sufficient for the targeted landing performance with near certainty. Even single-slotted flaps with dropped hinge kinematics will likely be insufficient if the geometric constrains for the trailing edge devices such as spanwise dimension, vertical hinge-line position, flap length remain in place. A slightly more sophisticated flap systems such as fixed-vane flaps with dropped hinge kinematics will however likely yield the targeted maximum lift coefficient of 2.5.

Additionally, the investigation leads to the following conclusions:

- The integration of the main landing gear fairing has a significant impact on the main wing's lift distribution. Considering the fairing within the basic wing design leads to a substantial improvement of the cruise flight performance.
- The nacelles' shape and vertical position are obviously important aspects with regard to L/D in cruise flight and maximum lift in low speed. The trends of both aspects are found to behave contrarily regarding cruise flight and high-lift performance. The selected shape and integration design therefore represents a compromise between the two performance metrics yielding acceptable low speed performance at moderate drag penalty. Besides additional potential for improvement that could be realized by more comprehensive studies, an increase in one of the performance metrics at the cost of the other one is easily achievable.
- Despite large variations in the mass flow rate of the cooling air depending on the flight phase and conditions, a fixed heat exchanger inlet appears to be feasible.
- Utilizing a high-lift optimization approach based on an extended non-linear lifting line method yields an increase in maximum lift of 7 % for the landing configuration compared to a design based on sectional 2D optimizations. The approach therefore represents a valuable compromise between the 2D optimization approach and a resource consuming 3D optimization with regard to high-lift design.
- Compared to the initial shape the final cruise flight shape yields an increase of approximately 11 % in L/D due to the 3D RANS studies.

References

[1] R. E. Wolleswinkel, R. de Vries, M. Hoogreef, and R. Vos, *A New Perspective on Battery-Electric Aviation, Part I: Reassessment of Achievable Range*. [Online]. Available: https://arc.aiaa.org/doi/abs/10.2514/6.2024-1489

[2] T. Gerhold, "Overview of the Hybrid RANS Code TAU," in *MEGAFLOW – Numerical Flow Simulation for Aircraft Design*, ser. Notes on Numerical Fluid Mechanics and Multidisciplinary Design. Springer, 2005, vol. 89, pp. 81–92.

[3] P. Spalart and S. Allmaras, "A One–Equation Turbulence Model for Aerodynamic–Flows," AIAA Paper 92–439, 1992.

[4] P. Spalart and M. Shur, "On the sensitization of turbulence models to rotation and curvature," ser. Aerospace Science and Technology, 1997, vol. 1, pp. 297–302.

[5] P. Spalart, "Strategies for turbulence modelling and simulations," *International Journal of Heat and Fluid Flow*, vol. 21, no. 3, pp. 252–263, 2000. [Online]. Available: https://www.sciencedirect.com/science/article/pii/S0142727X00000072

[6] A. Raichle, "Flux Conservative Discretization of the Actuator Disk Model as a Discontinuity Surface," Technical University Braunschweig, Braunschweig, Germany, Ph.D. Thesis, 2017.

[7] D. Keller, S. Spinner, A. Stuermer, and J. Park, "Assessment of Propeller Modeling Approaches for Aerodynamic Simulations," Rome, Italy, 2025, no. submitted.

[8] C. Lenfers, N. Beck, and M. Bauer, "Propeller and active high lift wing interaction in experiment and simulation," *New Results in Numerical and Experimental Fluid Mechanics X*, vol. 132, pp. 51–61, 2016.

[9] C. O. M. Gutierrez, A. Stürmer, C. Clemen, and A. Grimminger, "Validation of Actuator Disk Simulations of CROR Propulsion Systems at Low-Speed Flight Conditions," no. 2012-2787. New Orleans, USA: American Institute of Aeronautics and Astronautics, 2012, AIAA Paper.

[10] B. C. Systems, "Ansa pre processor," in [online web site], URL: https://www.beta-cae.com/ansa.htm, [retrieved 20th March 2025].

[11] A. Giuffré, R. de Vries, R. E. Wolleswinkel, and C. M. D. Servi, "Thermal management system architecture for the powertrain of a 90-seater battery-electric aircraft." AIAA Aviation Forum 2025.

[12] N. Herzog, D. Keller, and C. Breitsamter, "Two aerodynamic mid-fidelity approaches on a distributed propulsion wing," *Journal of Aircraft*, vol. 61, no. 1, pp. 196–210, 2024. [Online]. Available: https://doi.org/10.2514/1.C037313

[13] C. P. van Dam, J. C. V. Kam, and J. K. Paris, "Design-oriented high-lift methodology for general aviation and civil transport aircraft," *Journal of Aircraft*, vol. 38, no. 6, pp. 1076–1084, 2001. [Online]. Available: https://doi.org/10.2514/2.2875

[14] J. Weissinger, "Über eine Erweiterung der Prandtlschen Theorie der tragenden Linie," *Mathematische Nachrichten*, vol. 2, no. 1-2, pp. 45–106, 1949.

[15] S. Gallay and E. Laurendeau, "Preliminary-design aerodynamic model for complex configurations using lifting-line coupling algorithm," *Journal of Aircraft*, vol. 53, no. 4, pp. 1145–1159, 2016. [Online]. Available: https://doi.org/10.2514/1.C033460

[16] R. de Vries, R. E. Wolleswinkel, M. Hoogreef, and R. Vos, *A New Perspective on Battery-Electric Aviation, Part II: Conceptual Design of a 90-Seater*. [Online]. Available: https://arc.aiaa.org/doi/abs/10.2514/6.2024-1490

[17] J. Wild, J. Brezillon, O. Amoignon, J. Quest, F. Moens, and D. Quagliarella, "Advanced Design by Numerical Methods and Wind Tunnel Verification within the European High-Lift Program," *Journal of Aircraft*, vol. 46, pp. 157–167, 2009.

[18] D. Keller, "High-lift design for a forward swept natural laminar flow wing," *CEAS Aeronautical Journal*, vol. 11, pp. 81–92, Mai 2019. [Online]. Available: https://elib.dlr.de/131288/